

Cite this: *Nanoscale*, 2018, **10**, 8404Received 1st February 2018,  
Accepted 10th April 2018

DOI: 10.1039/c8nr00925b

rsc.li/nanoscale

# Polyoxometalate precursors for precisely controlled synthesis of bimetallic sulfide heterostructure through nucleation-doping competition†

Yu-Jia Tang, A-Man Zhang, Hong-Jing Zhu, Long-Zhang Dong,  Xiao-Li Wang, Shun-Li Li, Min Han,  Xiang-Xin Xu  and Ya-Qian Lan  \*

Molybdenum disulfide ( $\text{MoS}_2$ )-based bimetallic sulfides have drawn increasing research attention because of their unique structures and properties. Herein, a one-pot hydrothermal synthesis method is proposed to grow a series of bimetallic sulfides on carbon cloth ( $\text{M-Mo-S/CC}$ ,  $\text{M} = \text{Co}, \text{Ni}, \text{Fe}$ ) using Anderson-type polyoxometalates (POMs) as bimetallic sources for the first time. An ideal model of  $\text{M-Mo-S/CC}$  was used to study the growth process through the nucleation-doping competition mechanism. It is proved for the first time that  $\text{M-Mo-S/CC}$  possess certain compositions of bimetallic sulfides rather than metal doped  $\text{MoS}_2$  structures because the nucleation reaction is predominant in the nucleation-doping competition. Moreover, the nucleation rates of different metals can be compared to study the different morphologies of  $\text{M-Mo-S/CC}$  because Anderson-type POMs have fixed bimetal proportions and precise structures.  $\text{Co-Mo-S}$  and  $\text{Ni-Mo-S}$  show spherical heterostructures with  $\text{CoS}_2$  or  $\text{NiS}$  mainly inside and interconnected  $\text{MoS}_2$  nanosheets outside, while  $\text{Fe-Mo-S}$  exhibits uniform nanosheet morphology without stacking. As electrodes for alkaline water electrolysis,  $\text{M-Mo-S/CC}$  with different compositions and morphologies exhibit a variety of activities. Particularly, among the  $\text{M-Mo-S/CC}$  samples,  $\text{Co-Mo-S/CC}$  achieves the best performance for hydrogen evolution reaction, oxygen evolution reaction and overall water splitting. This study presents a facile strategy of using POMs as bimetallic precursors for studying the growth mechanism as well as the water electrolysis performances of  $\text{MoS}_2$ -based bimetallic sulfides.

## Introduction

Electrochemical water splitting for obtaining hydrogen ( $\text{H}_2$ ) and oxygen ( $\text{O}_2$ ) is one of the promising and environmentally

friendly steps in developing a possible hydrogen source.<sup>1</sup> In general, overall water splitting (OWS) involving hydrogen evolution reaction (HER) and oxygen evolution reaction (OER) is a thermodynamically unfavorable process, which requires highly-efficient electrocatalysts to reduce the overpotential and accelerate reaction kinetics.<sup>2,3</sup> Thus far, the benchmark electrocatalysts are commercial platinum (Pt) for HER and iridium oxide ( $\text{IrO}_2$ ) or ruthenium oxide ( $\text{RuO}_2$ ) for OER.<sup>4</sup> These noble metal-based catalysts have excellent activity, but their low natural abundance and high cost significantly limit the commercialization.<sup>5,6</sup> Therefore, great efforts have been made to synthesize non-noble metal-based electrocatalysts such as sulfides,<sup>7,8</sup> carbides,<sup>9</sup> phosphides,<sup>10,11</sup> oxides<sup>12,13</sup> and carbon-based metal-free materials<sup>14</sup> for water splitting.

Molybdenum disulfide ( $\text{MoS}_2$ ), a typical example of two-dimensional (2D) transition-metal dichalcogenides (TMDs), has attracted wide research interest owing to its graphene-like structure.<sup>15,16</sup> An increasing number of computational and experimental studies indicate that  $\text{MoS}_2$  is a promising material for various applications, such as energy storage and conversion<sup>17–19</sup> and sensing.<sup>20,21</sup> In particular,  $\text{MoS}_2$  has been traditionally found to be an excellent HER electrocatalyst in acidic electrolytes, but is seldom investigated in alkaline medium due to its poor stability and poor catalytic ability for OER. It is worth noting that hybridization of  $\text{MoS}_2$  by introducing a secondary transition metal to form a  $\text{MoS}_2$ -based bimetallic sulfide can regulate the morphology and structure, thus enhancing the relevant properties.<sup>22–24</sup> Thus far, many ways have been reported for preparing  $\text{MoS}_2$ -based materials including exfoliation method, chemical vapor deposition (CVD) method and wet chemical synthesis method.<sup>15,25</sup> Wet chemical synthesis methods can be divided into two types: one-pot hydrothermal synthesis and multiple step synthesis. Multiple step synthesis can be used to obtain a metal sulfide/ $\text{MoS}_2$  composite with certain composition and special morphology, such as nanosphere and nanosheet, which can significantly improve OER and even OWS performance.<sup>26–28</sup> However, the synthesis of this type of  $\text{MoS}_2$ -based bimetallic

Jiangsu Collaborative Innovation Centre of Biomedical Functional Materials, Jiangsu Key Laboratory of New Power Batteries, School of Chemistry and Materials Science, Nanjing Normal University, Nanjing 210023, China. E-mail: yqlan@njnu.edu.cn

† Electronic supplementary information (ESI) available: Experimental methods, SEM, TEM, PXRD, FT-IR, Raman, LSV, EIS, tables and so on. See DOI: 10.1039/c8nr00925b

sulfide always needs multi-step reactions, harsh experimental conditions and high energy cost, making the study of the growth mechanism more complex and difficult.

Till date, the one-pot hydrothermal synthesis method has been largely applied to synthesize MoS<sub>2</sub>-based bimetallic sulfides due to the advantages of low-cost, simple steps and high yield. However, most reported products are transition metal-doped MoS<sub>2</sub> materials. The existence and coordination forms of these transition metals-doped MoS<sub>2</sub> structures are still ambiguous and are often simulated and engineered by theoretical methods.<sup>29,30</sup> Although transition metal doped MoS<sub>2</sub> materials as water splitting electrocatalysts have been extensively discussed, there is no report on growth mechanism studies to clarify the reasons for formation of specific morphologies and heterostructures. In addition, metal-doped MoS<sub>2</sub> materials usually have specific compositions of MoS<sub>2</sub> as identified through powder X-ray diffraction (PXRD) characterization, but no other peak information for doping metals could be obtained. If metal-doped MoS<sub>2</sub> materials show broad diffraction peaks for the low crystallinity MoS<sub>2</sub> prepared at relatively low hydrothermal temperatures, it may cover the peaks of other transition metal sulfides. Therefore, so far, the exact compositions of MoS<sub>2</sub>-based materials still remain controversial and lack research into the growth mechanism. In our view, MoS<sub>2</sub>-based materials prepared by the one-pot hydrothermal synthesis method not only show the existence of metal doped into the MoS<sub>2</sub> structure, but can also form transition metal sulfides coupled with MoS<sub>2</sub>. During the hydrothermal process, the doping reaction and nucleation reaction must co-exist, which directly affects the final composition due to nucleation-doping competition. If the nucleation reaction dominates the hydrothermal process, metal sulfides/MoS<sub>2</sub> composite with certain compositions will be formed, otherwise metal doped MoS<sub>2</sub> will be primarily obtained. Therefore, designing a suitable experimental platform to study the nucleation-doping competition of MoS<sub>2</sub>-based materials by the one-pot hydrothermal synthesis has great research significance.

Herein, we report a facile one-pot strategy for the synthesis of a new class of M-Mo-S nanosheets (M = Co, Ni, Fe) on carbon cloth without any binders (M-Mo-S/CC). The as-synthesized M-Mo-S contains two certain sulfides (MoS<sub>2</sub> and MS<sub>x</sub>) when Anderson-type polyoxometalates (POMs) and thiourea (TU) are used as bimetallic and sulfur sources, respectively. POMs, with size the nanometer scale are a subset of early transition metal-oxygen clusters with unique physicochemical properties.<sup>31</sup> Anderson-type POMs, represented by the formula [XM<sub>6</sub>O<sub>24</sub>H<sub>x</sub>]<sup>n-</sup> (X = Zn, Cu, Co, Ni, Fe, etc., M = Mo), exhibit a planar structure formed by a metal-oxygen octahedral cavity at the center and six octahedral MO<sub>6</sub> at the periphery.<sup>32</sup> Anderson-type POMs not only possess precise structure, nanoscale size (<1 nm) and good water solubility, but can also provide fixed proportions of bimetallic sources, which are the optimal precursors for the controlled synthesis of M-Mo-S/CC with specific morphology and structure. Therefore, M-Mo-S/CC could be the ideal system to study the growth mechanism based on nucleation-doping competition. Since

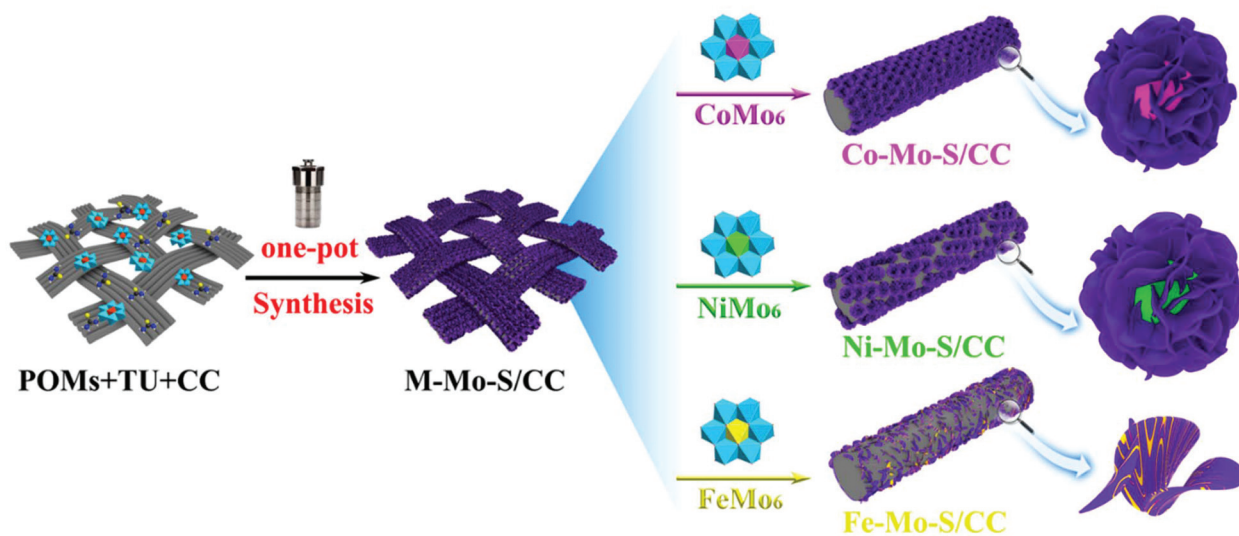
the nucleation reaction plays a dominant role during the hydrothermal process, M-Mo-S/CC systems show certain compositions with distinct morphologies because different transition metals have different nucleation rates. Moreover, the water electrolysis properties of M-Mo-S/CC are discussed. In alkaline medium, Co-Mo-S/CC achieves overpotentials of 118 mV and 300 mV vs. RHE at current density of 10 mA cm<sup>-2</sup> for HER and OER, respectively, which reveals the best performance among M-Mo-S/CC that is comparable to most reported MoS<sub>2</sub>-based electrocatalysts. When applying Co-Mo-S/CC electrodes as both anode and cathode in an advanced alkaline water electrolyzer, a cell voltage of only 1.80 V is required to deliver high current density of 50 mA cm<sup>-2</sup>.

## Results and discussion

### Synthesis and characterization of M-Mo-S/CC

The detailed synthesis process is illustrated in Scheme 1. A one-pot synthesis approach was applied to prepare M-Mo-S/CC using POMs and TU as precursors. First, the successful preparations of the three Anderson-type POMs were proved by X-ray crystallographic data, Fourier transform infrared spectroscopy (FT-TR) and PXRD characterizations (Fig. S1, S2 and Table S1, ESI†). Taking Co-Mo-S/CC as an example, (NH<sub>4</sub>)<sub>4</sub>[Co(II)Mo<sub>6</sub>O<sub>24</sub>H<sub>6</sub>].6H<sub>2</sub>O POMs (CoMo<sub>6</sub>) was selected as the bimetallic precursor and sonicated together with TU in water for 30 min. The above solution was transferred to a Teflon-lined stainless-steel autoclave with two pieces of CC (1 × 2 cm<sup>2</sup>). After hydrothermal reaction at 200 °C for 24 h, Co-Mo-S/CC can be obtained with Co-Mo-S nanospheres uniformly dispersed on CC (mass loading is ca. 1 mg cm<sup>-2</sup>) (Fig. S3, ESI†). In addition, (NH<sub>4</sub>)<sub>4</sub>[Ni(II)Mo<sub>6</sub>O<sub>24</sub>H<sub>6</sub>].5H<sub>2</sub>O (NiMo<sub>6</sub>) and (NH<sub>4</sub>)<sub>3</sub>[Fe(III)Mo<sub>6</sub>O<sub>24</sub>H<sub>6</sub>].6H<sub>2</sub>O (FeMo<sub>6</sub>) were chosen to prepare Ni-Mo-S/CC and Fe-Mo-S/CC, respectively. Ni-Mo-S exhibited similar morphology to Co-Mo-S but with uneven coverage on CC, while Fe-Mo-S nanosheets directly grew on CC without stacking. Sodium molybdate (Na<sub>2</sub>MoO<sub>4</sub>) was used instead of POMs as the single Mo source to prepare MoS<sub>2</sub>/CC for comparison. Energy dispersive X-ray (EDS) spectra (Fig. S4, ESI†) show the existence of M (Co, Ni, Fe), Mo and S, suggesting the successful synthesis of M-Mo-S/CC. On the basis of inductively coupled plasma (ICP) and EDS analysis, the molar ratios of M and Mo for M-Mo-S/CC were all between 1:3.2 and 1:3.5.

Different morphologies and structures of M-Mo-S/CC can be characterized by scanning electron microscopy (SEM). First, pure CC (Fig. S5, ESI†) was observed, with 3D carbon fiber network and fibrous morphology. After hydrothermal treatment, the SEM image of Co-Mo-S/CC (Fig. 1a) exhibits thin nanosheets stacked into small-sized spheres and grown on CC uniformly and densely. To gain more details of the morphology, SEM images captured at different scales were also characterized. According to the magnified SEM image of Co-Mo-S/CC, the spheres stacked by nanosheets are uniform with a diameter of approximately 1 μm. In contrast, the SEM image



**Scheme 1** Illustration of the preparation of M-Mo-S/CC (M = Co, Ni, Fe).

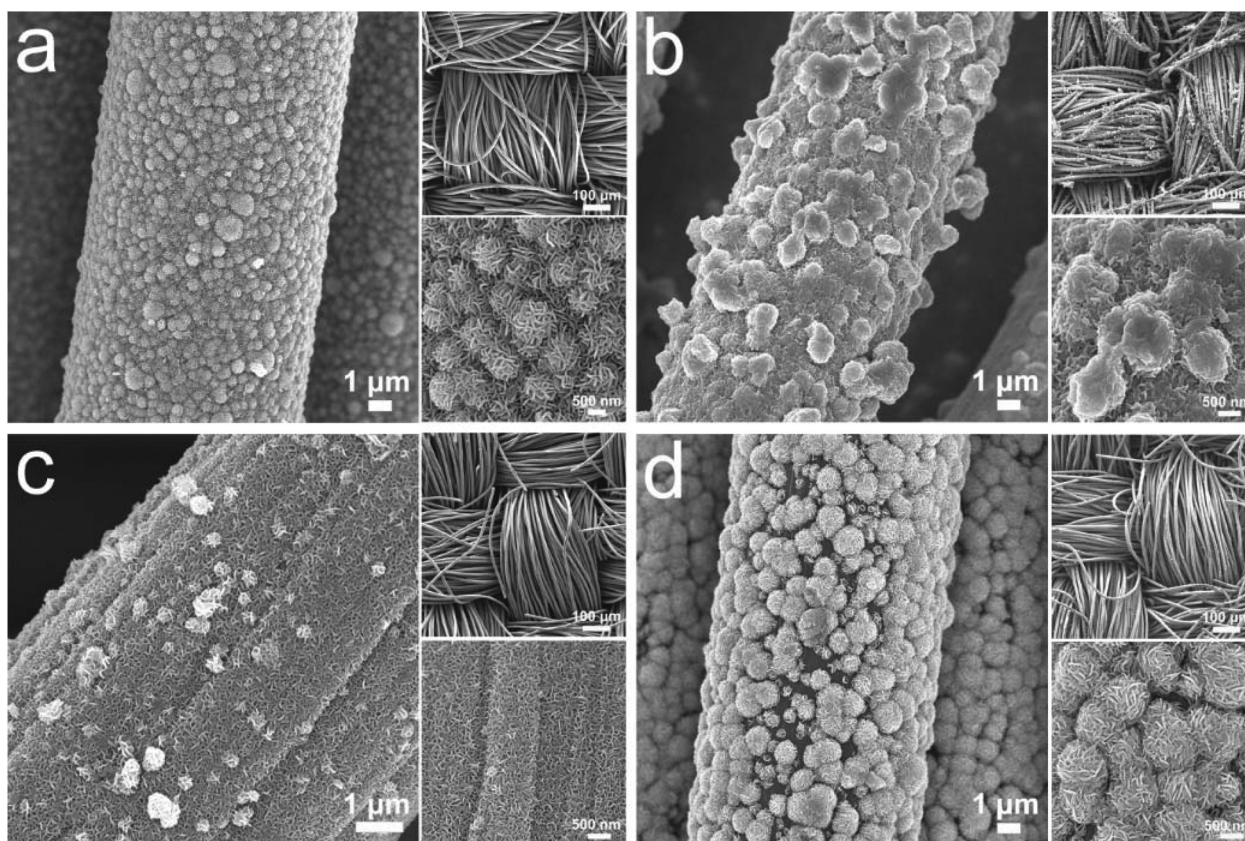


**Fig. 1** SEM images of (a) Co-Mo-S/CC, (b) Ni-Mo-S/CC, (c) Fe-Mo-S/CC and (d) MoS<sub>2</sub>/CC at different scales.

of Ni-Mo-S/CC (Fig. 1b) presents micro-sized crumpled particles distributed unevenly on CC. The relevant low and high magnification SEM images show that CC is covered with thick Ni-Mo-S of different sizes. When FeMo<sub>6</sub> was used to prepare Fe-Mo-S/CC, interconnected Fe-Mo-S nanosheets stack

directly on CC, as displayed in Fig. 1c. SEM image of MoS<sub>2</sub>/CC (Fig. 1d) demonstrates that MoS<sub>2</sub> spheres with various sizes are unevenly grown on CC and unable to totally cover the surface of CC. TEM images of M-Mo-S sonicated from CC substrates are shown in Fig. S6, ESI† and are in accordance with



the SEM results. Moreover, PXRD was used to investigate the phase compositions of M-Mo-S. PXRD analysis of Co-Mo-S provides the diffraction patterns, in accordance with those of simulated MoS<sub>2</sub> (JCPDS 65-1941) and cobalt sulfide (CoS<sub>2</sub>, JCPDS 65-3322) (Fig. S7a, ESI†). The sharp peaks of Ni-Mo-S are in agreement with those of simulated MoS<sub>2</sub> and nickel sulfide (NiS, JCPDS 75-613) (Fig. S7b, ESI†), while the peaks of Fe-Mo-S agreed with those of simulated MoS<sub>2</sub> and iron sulfide (FeS, JCPDS 65-9124) (Fig. S7c, ESI†). PXRD pattern of MoS<sub>2</sub> without metal doping (Fig. S7d, ESI†) exhibits the characteristic diffraction peaks assigned to the typical hexagonally symmetric structured MoS<sub>2</sub>.<sup>33</sup>

Raman spectra (Fig. S8, ESI†) of M-Mo-S/CC and MoS<sub>2</sub>/CC samples were used to prove the existence of pristine MoS<sub>2</sub> nanosheets that show the typical in-plane E<sub>2g</sub> and out-of-plane A<sub>1g</sub> peaks of MoS<sub>2</sub>. The specific surface area and porosity of M-Mo-S/CC were characterized *via* N<sub>2</sub> adsorption-desorption isotherms and pore size distributions (Fig. S9, ESI†). In addition, X-ray photo-electron spectroscopy (XPS) analysis was used to study the composition and surface chemical state of M-Mo-S/CC (Fig. S10, ESI†). Co 2p spectrum of Co-Mo-S/CC (Fig. S11a, ESI†) presents four main peaks of Co<sup>2+</sup> 2p<sub>1/2</sub>, Co<sup>3+</sup> 2p<sub>1/2</sub>, Co<sup>2+</sup> 2p<sub>3/2</sub> and Co<sup>3+</sup> 2p<sub>3/2</sub> at 796.5, 793.9, 780.7 and 779.6 eV, respectively, with satellite peaks at higher energy, indicating the coexistence of Co<sup>2+</sup> and Co<sup>3+</sup> in Co-Mo-S/CC.<sup>34</sup> Three peaks in the Mo 3d spectrum (Fig. S11b, ESI†) centered at 235.8, 232.4 and 228.8 eV are ascribed to Mo<sup>6+</sup> 3d<sub>3/2</sub>, Mo<sup>4+</sup> 3d<sub>3/2</sub> and Mo<sup>4+</sup> 3d<sub>5/2</sub>, respectively, which are typical for MoS<sub>2</sub> and partially surface-oxidized MoO<sub>x</sub>. The S 2s binding energy peak (225.8 eV) is also close to that of Mo 3d. The S 2p spectrum (Fig. S11c, ESI†) can be deconvoluted into two component peaks: S 2p<sub>1/2</sub> (162.8 eV) and S 2p<sub>3/2</sub> (161.6 eV). The C 1s spectrum, mainly derived from CC (Fig. S11d, ESI†), can be deconvoluted into two peaks: C-C/C=C (284.6 eV) and C-O (285.2 eV) bonds. The N 1s spectrum (Fig. S11e, ESI†) demonstrates two types of N species, namely, graphitic N and pyridinic N, which are located at 401.1 and 398.3 eV, respectively. The intense peak at 394.6 eV is attributed to the Mo-N bond. The O 1s spectrum in Fig. S11f, ESI† shows three peaks of C-OH (532.1 eV), C-O/C=O (531.2 eV) and Mo-O (530.4 eV) bonds, which are the oxygen-containing groups of Co-Mo-S/CC.<sup>35</sup> For comparison, the XPS spectra of contrast samples are analyzed in Fig. S12-S14, ESI†.

### Growth mechanism study of M-Mo-S/CC

To understand the morphology and composition evolution, M-Mo-S/CC-*t* samples (*t* = 3 h, 6 h, 10 h and 24 h) obtained at different time intervals were observed by SEM and PXRD. Taking Co-Mo-S/CC as an example, after reacting at 200 °C for 3 h, the SEM image of Co-Mo-S/CC-3 h shows irregular structures entirely coating CC (Fig. 2a). When the reaction time was extended to 6 h, a number of nanosheets started to grow epitaxially at the outer irregular surface, according to the SEM image in Fig. 2b. With an increase in the hydrothermal time to 10 h, uniform-sized spheres stacked by nanosheets began growing on CC (Fig. 2c). Both the number and thickness of

these pellets continued to increase and arrange on CC tightly and regularly as the hydrothermal reaction proceeded up to 24 h. The PXRD patterns (Fig. 2d) are also in accordance with the SEM images. In the first three hours, there are only two characteristic broad peaks of Co-Mo-S/CC-3 h at 26.5° and 43.3°, assigned to the CC substrate. After reacting for 6 h, all the weak diffraction peaks in the PXRD pattern of Co-Mo-S/CC-6 h matched well with the CoS<sub>2</sub> phase. Notably, there is a new peak at 14.4° ascribed to the (002) plane of MoS<sub>2</sub>, accompanied by intensity increase of CoS<sub>2</sub> peaks until the hydrothermal reaction is carried out for 10 h. After 24 h of hydrothermal reaction, the PXRD pattern of Co-Mo-S/CC-24 h shows new peaks emerging at 14.4°, 33.6°, 39.5° and 59.1°, which are assigned to the (002), (100), (103) and (110) planes of hexagonally symmetrically structured MoS<sub>2</sub>. Additionally, the peak intensity of CoS<sub>2</sub> enhanced gradually with the increase in reaction time (Fig. 2d), suggesting that some CoS<sub>2</sub> can still be nucleated even when MoS<sub>2</sub> nanosheets start to form outside the particles. Consequently, previously formed CoS<sub>2</sub> on CC can serve as structural backbones to provide active sites for the further growth of MoS<sub>2</sub> to form Co-Mo-S heterostructures with CoS<sub>2</sub> nanospheres mainly inside and MoS<sub>2</sub> nanosheets intercrossed outside the heterostructure.<sup>36</sup> To clearly describe the growth process, the simulated morphologies of individual Co-Mo-S particles obtained at different time intervals are presented in Fig. 2e. Furthermore, the aberration-corrected high-angle annular dark field (HAADF) image, EDS elemental mappings and overlay image of Co-Mo-S obtained at 24 h (Fig. 2f) demonstrate the homogenous distribution of Mo but central aggregate distribution of Co, further implying a heterostructure with CoS<sub>2</sub> particles coated by MoS<sub>2</sub> nanosheets. The growth process of Ni-Mo-S/CC is similar to that of Co-Mo-S/CC (Fig. S15, ESI†). NiS can be formed at the early stage (3 h) and serve as a substrate for the growth of MoS<sub>2</sub>. When the reaction time reached 6 h, MoS<sub>2</sub> aggregates with diverse sizes started to grow outside NiS particles randomly to form Ni-Mo-S heterostructures, which are consistent with the element mappings. In contrast, Fe-Mo-S/CC shows a totally different growth process. Fe-Mo-S can be synthesized at the early stage (3 h) with FeS and MoS<sub>2</sub> nanosheets growing simultaneously on CC without aggregates (Fig. S16, ESI†). When the reaction time increased, the morphology and composition of Fe-Mo-S remained unchanged. Fe-Mo-S nanosheets only grew thicker and the intensity of peaks increased according to SEM and PXRD characterizations. The EDX mappings also show uniform distributions of Fe, Mo and S elements.

It seems that Anderson-type POMs as bimetallic sources have direct effects on the formation of M-Mo-S/CC with different morphologies and structures, which can be explained by the nucleation-doping competition mechanism as follows. In an M-Mo-S/CC system, the nucleation rates are much faster than the doping rates, thus producing bimetallic sulfides with certain compositions. Although M-Mo-S contain similar compositions of MS<sub>x</sub>/MoS<sub>2</sub>, they show different structures and morphologies due to their different nucleation rates. In Co-

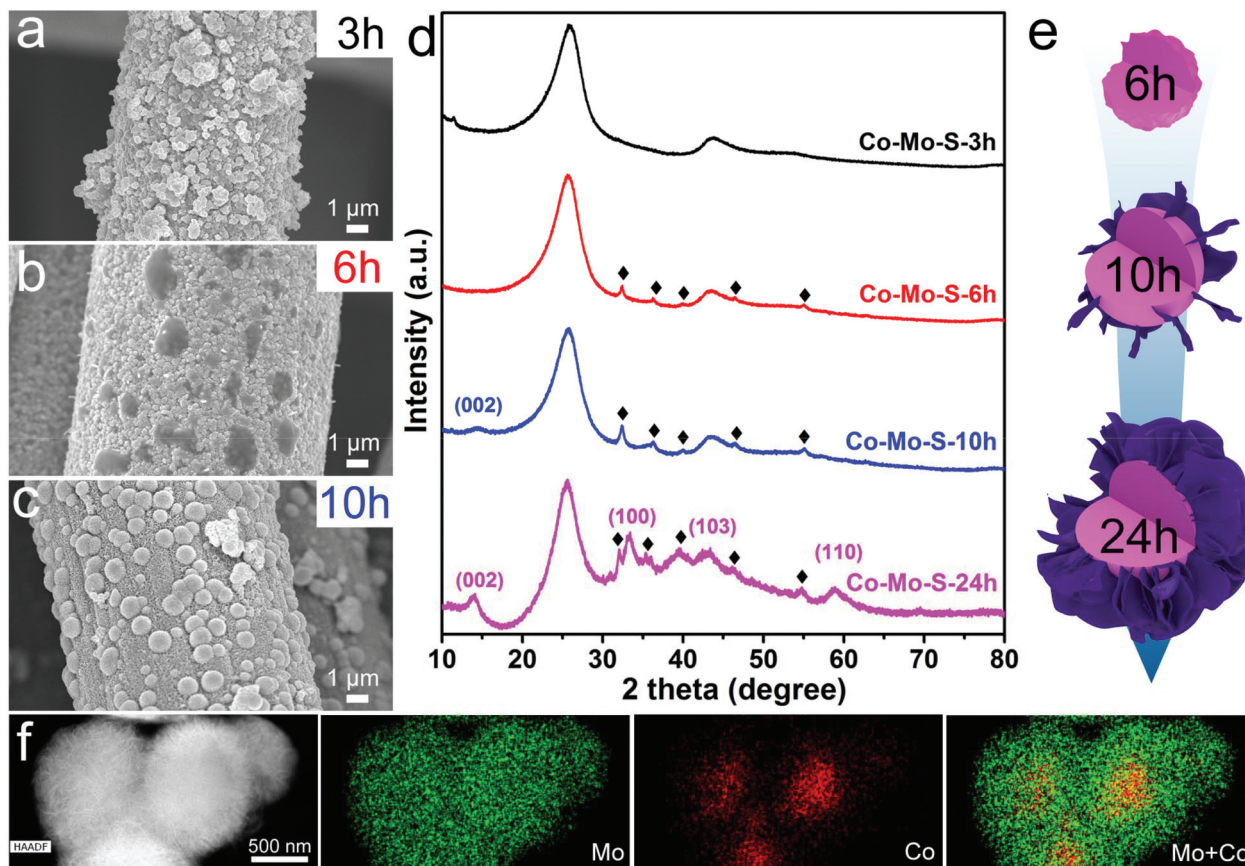


**Fig. 2** (a–c) SEM images of Co–Mo–S/CC-*t* (*t* = 3 h, 6 h and 10 h) obtained at different hydrothermal times. (d) PXRD spectra of Co–Mo–S/CC-*t* obtained at different hydrothermal times (♦ represents the peaks of CoS<sub>2</sub>). (e) Simulated images for the growth process of individual Co–Mo–S nanospheres. (f) Aberration-corrected HAADF image and corresponding elemental mappings of Co–Mo–S and overlay image of Co and Mo elements. Mo is shown in green and Co is shown in red.

Mo–S, S<sup>2−</sup> ions can be quickly released from TU during the hydrothermal process and react preferentially with Co<sup>2+</sup> ions to nucleate CoS<sub>2</sub> particles on the rough CC surface *via* the van der Waals interaction. Then, excess S<sup>2−</sup> ions continuously react with Mo<sup>6+</sup> from CoMo<sub>6</sub> distributed around CoS<sub>2</sub> particles, leading to the continued epitaxial nucleation of MoS<sub>2</sub> nanosheets outside CoS<sub>2</sub>. Because of the existence of excess S sources, Co and Mo ions would prefer to nucleate and grow into Co–Mo–S nanospheres. In addition, the ionic radius of Co<sup>2+</sup> (74 pm) is larger than that of Mo<sup>6+</sup> (62 pm), so that the outward diffusion rate of Co<sup>2+</sup> is much slower than that of Mo<sup>6+</sup>. Although the Co/Mo molar ratio is 1:6 in the CoMo<sub>6</sub> precursor, the nucleation reaction to form CoS<sub>2</sub> still takes preference during the nucleation-doping competition. Moreover, from the thermodynamics perspective, smaller solubility product constant (*K*<sub>sp</sub>) implies better stability of the sulfide. Compared with that of CoS<sub>2</sub> ( $3 \times 10^{-26}$ ), the smaller *K*<sub>sp</sub> of MoS<sub>2</sub> ( $2.2 \times 10^{-56}$ ) confirms its good stability.<sup>37,38</sup> Therefore, Co–Mo–S with heterostructures of CoS<sub>2</sub> mainly inside and MoS<sub>2</sub> outside is preferentially formed due to the higher thermodynamic stability of MoS<sub>2</sub> than CoS<sub>2</sub>.

The growth mechanism of Ni–Mo–S could be explained similarly to that of the Co–Mo–S system because of the similarity in the ionic radius of Ni<sup>2+</sup> (72 pm) with that of Co<sup>2+</sup> and the larger *K*<sub>sp</sub> of NiS ( $3.2 \times 10^{-19}$ ) than that of MoS<sub>2</sub>. However, Fe–Mo–S with homogeneous nanosheet structures exhibits a different growth mechanism because Fe<sup>3+</sup> and Mo<sup>6+</sup> both have the same nucleation rates with S<sup>2−</sup> ions. Similar ionic radii of Fe<sup>3+</sup> (64 pm) and Mo<sup>6+</sup> (62 pm) also accelerate the nucleation reaction, making FeS and MoS<sub>2</sub> nanosheets grow simultaneously on CC. The *K*<sub>sp</sub> of FeS is  $6.3 \times 10^{-18}$ , which is also much larger than that of MoS<sub>2</sub>. Although FeS and MoS<sub>2</sub> show the same nucleation rates, the content of MoS<sub>2</sub> is higher than that of FeS, suggesting that Fe–Mo–S nanosheets still have a relatively stable structure. In contrast, the size of MoS<sub>2</sub> spheres on CC varies because epitaxial nucleation occurs at different rates at different sites on rough CC when using Na<sub>2</sub>MoO<sub>4</sub> as the single Mo source. The CC surface exhibits randomly allocated striations, which hinder the epitaxial growth of MoS<sub>2</sub> sheets and lead to formation of wrinkles and stacked pellets with irregular sizes to some extent.<sup>30</sup> Therefore, the nucleation-doping competition mechanism plays an important role



in synthesizing M-Mo-S with different morphologies and structures.

Co-Mo-S was characterized by high-resolution TEM (HRTEM). The evident lattice fringe with interlayer spacing of 0.62 nm (Fig. 3a) is directly indexed to the (002) plane of typical 2H-MoS<sub>2</sub>. As shown in Fig. 3b, the lattice fringe of 0.273 nm demonstrates that the (100) and (010) planes of MoS<sub>2</sub> are exposed with active Mo and S edges. Another type of lattice fringe with lattice spacing of 0.276 nm corresponds to the (200) plane of CoS<sub>2</sub>, suggesting the successful hybridization of MoS<sub>2</sub> and CoS<sub>2</sub> in Co-Mo-S.<sup>26</sup> The HRTEM image of Ni-Mo-S (Fig. 3c) reveals that the lattice spacing of 0.296 nm is in accordance with the (100) plane of NiS. In addition, the lattice spacing of 0.273 nm between NiS nanosheets is assigned to the (100) and (010) planes of MoS<sub>2</sub>, further proving the heterostructure of Ni-Mo-S. The HRTEM image of Fe-Mo-S (Fig. 3d) displays lattice fringes of 0.62 nm and 0.284 nm corresponding to the (002) plane of MoS<sub>2</sub> and the (002) plane of FeS, respectively. Pure MoS<sub>2</sub> nanosheets were also characterized by HRTEM and EDX mapping for comparison (Fig. S17, ESI†).

### Electrocatalytic HER and OER performance of M-Mo-S/CC

The HER performance was first investigated in N<sub>2</sub>-saturated 1 M KOH electrolyte using M-Mo-S/CCs as direct working electrodes. For comparison, the linear sweep voltammogram (LSV) curves of Co-Mo-S/CC, Ni-Mo-S/CC, Fe-Mo-S/CC, MoS<sub>2</sub>/CC and commercial 20% Pt/C were studied with 85% *iR*-compensation. The bare CC electrode was tested and showed poor HER and OER performances (Fig. S18, ESI†). As shown in Fig. 4a, Co-Mo-S/CC affords an onset overpotential of *ca.*

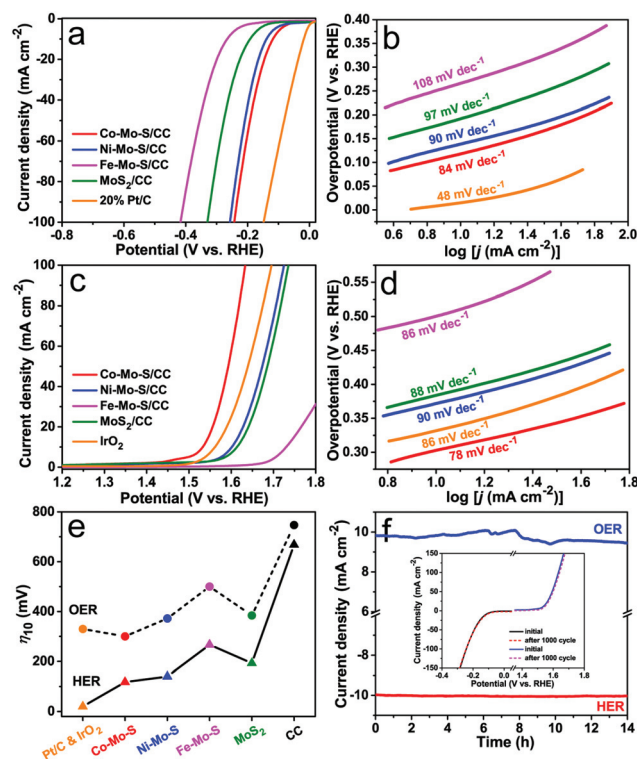


**Fig. 4** (a) LSV curves of Co-Mo-S/CC, Ni-Mo-S/CC, Fe-Mo-S/CC, MoS<sub>2</sub>/CC and 20% Pt/C for HER. (b) Corresponding Tafel plots for HER. (c) LSV curves of Co-Mo-S/CC, Ni-Mo-S/CC, Fe-Mo-S/CC, MoS<sub>2</sub>/CC and IrO<sub>2</sub> for OER. (d) Corresponding Tafel plots for OER. (e) Overpotential to achieve current density of 10 mA cm<sup>-2</sup>. (f) Chronoamperometric curves of Co-Mo-S/CC at overpotential of 120 mV vs. RHE for HER and 300 mV vs. RHE for OER, for 14 h. Inset: LSV curves for Co-Mo-S/CC before and after 1000 CV cycles.

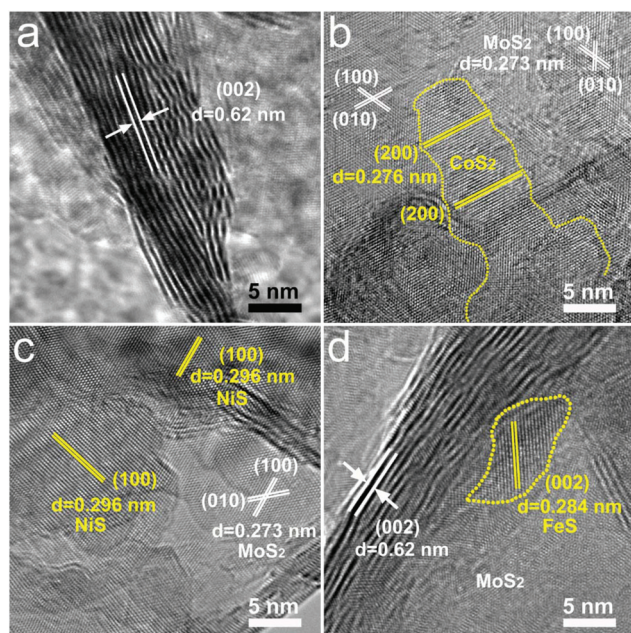


**Fig. 3** (a), (b) HRTEM images of Co-Mo-S. (c) HRTEM image of Ni-Mo-S. (d) HRTEM image of Fe-Mo-S.

60 mV vs. RHE, approaching the commercial 20% Pt/C catalyst, which is more positive than those of Ni-Mo-S/CC (78 mV), Fe-Mo-S/CC (170 mV), and MoS<sub>2</sub>/CC (126 mV). Tafel slope is a well-known parameter to represent the reaction kinetics of water electrolysis. Unlike 20% Pt/C (48 mV dec<sup>-1</sup>), Co-Mo-S/CC exhibits enhanced HER electrocatalytic activity, yielding a small Tafel slope of 84 mV dec<sup>-1</sup>, which is much better than those of Ni-Mo-S/CC (90 mV dec<sup>-1</sup>), Fe-Mo-S/CC (108 mV dec<sup>-1</sup>) and MoS<sub>2</sub>/CC (97 mV dec<sup>-1</sup>) (Fig. 4b). Moreover, OER performance was measured under the same alkaline conditions. In particular, Co-Mo-S/CC (Fig. 4c) delivered the smallest onset overpotential and increasing oxygen-evolution current among the contrast samples. The Tafel slope of Co-Mo-S/CC (Fig. 4d) is 78 mV dec<sup>-1</sup>, which is the smallest among the values of 90 mV dec<sup>-1</sup> for Ni-Mo-S/CC, 86 mV dec<sup>-1</sup> for Fe-Mo-S/CC, 88 mV dec<sup>-1</sup> for MoS<sub>2</sub>/CC and 86 mV dec<sup>-1</sup> for commercial IrO<sub>2</sub>. Such good HER and OER performances of Co-Mo-S/CC largely depend on the active CoS<sub>2</sub> and MoS<sub>2</sub> species, unique heterostructures and fast electron transfer abilities in alkaline electrolyte.

The overpotential at current density of 10 mA cm<sup>-2</sup> (η<sub>10</sub>) is an important parameter for both HER and OER, which is a

metric benchmark for solar fuel synthesis.<sup>2</sup> According to the LSV curves,  $\eta_{10}$  of Co-Mo-S/CC is only 118 mV *vs.* RHE for HER and 300 mV *vs.* RHE for OER. In Fig. 4e, excluding commercial 20% Pt/C catalyst (20 mV),  $\eta_{10}$  of Co-Mo-S/CC for HER is smaller than all samples including Ni-Mo-S/CC (140 mV), Fe-Mo-S/CC (267 mV) and MoS<sub>2</sub>/CC (193 mV). For OER,  $\eta_{10}$  of Co-Mo-S/CC is the smallest among all contrast samples including Ni-Mo-S/CC (370 mV), Fe-Mo-S/CC (500 mV), MoS<sub>2</sub>/CC (380 mV) and even commercial IrO<sub>2</sub> catalyst (330 mV). Such low  $\eta_{10}$  values of Co-Mo-S/CC are comparable to those of most reported sulfide-based materials and other non-noble-metal-based catalysts for both HER (Table S2†) and OER (Table S3†) such as Co/Co<sub>9</sub>S<sub>8</sub>@SNGS,<sup>39</sup> Ni<sub>3</sub>S<sub>2</sub>/NF,<sup>40</sup> CoMoS<sub>x</sub>,<sup>41</sup> and Co<sub>3</sub>S<sub>4</sub>.<sup>42</sup> Additionally, LSV curves and calculated Tafel slopes of Co-Mo-S/CC and the contrast samples measured in 0.5 M H<sub>2</sub>SO<sub>4</sub> are shown and analyzed in Fig. S19, ESI.†

Stability was tested to reflect the durable operation of the electrocatalyst for water electrolysis. First, LSV curves before and after 1000 cyclic voltammetry (CV) cycles were recorded to examine the stability in alkaline medium. The inset in Fig. 4f contains the LSV curves of Co-Mo-S/CC before and after 1000 CV cycles, which exhibit almost no deactivation for both HER and OER. Moreover, chronoamperometry (CA) of Co-Mo-S/CC shows no current loss for HER and only about 4.0% drop in current density for OER, which occurred at constant overpotentials of 120 and 300 mV *vs.* RHE, respectively, over 14 h (Fig. 4f). The stabilities of the other three samples were also measured and are shown in Fig. S20, ESI.† The LSV curves of Ni-Mo-S/CC, Fe-Mo-S/CC and MoS<sub>2</sub>/CC before and after 1000 CV cycles exhibit slight deactivation for HER but significant decrease in OER activity. In addition, CA tests of contrast samples for HER show almost no degradation after 14 h operation. However, during OER stability performance, MoS<sub>2</sub>/CC lost more than 30.8% of its initial current density, while 90.5% current density retention of Ni-Mo-S/CC and even 22.3% increase in current density of Fe-Mo-S/CC were observed (Table S4†). Thus, the morphology and structure of M-Mo-S/CC have great effects on their stability performance. These results indicate that the nucleation reaction to form MoS<sub>2</sub>-based bimetallic sulfide, particularly Co-Mo-S, can improve the activity and stability toward electrochemical water splitting.

To gain further insight into the activity, we conducted electrochemical impedance spectroscopy (EIS) measurements at overpotential of 150 mV for HER and 300 mV for OER in 1 M KOH.<sup>43</sup> The Nyquist plots (Fig. S21, ESI†) of M-Mo-S/CC show distinct semicircles referring to the charge transfer resistance ( $R_{ct}$ ).  $R_{ct}$  of Co-Mo-S is only 9.3  $\Omega$  for HER and 4.9  $\Omega$  for OER *via* circuit simulation, which are smaller than those of Ni-Mo-S/CC, Fe-Mo-S/CC and MoS<sub>2</sub>/CC (Table S5†). More importantly, the electrochemically active surface area (ECSA) was evaluated by determining the electrochemical double-layer capacitance ( $C_{dl}$ ) (Fig. S22, ESI†).<sup>44</sup>  $C_{dl}$  of Co-Mo-S/CC is 50.6 mF cm<sup>-2</sup>, which is higher than those of Ni-Mo-S/CC (35.7 mF cm<sup>-2</sup>), Fe-Mo-S/CC (15.1 mF cm<sup>-2</sup>) and MoS<sub>2</sub>/CC

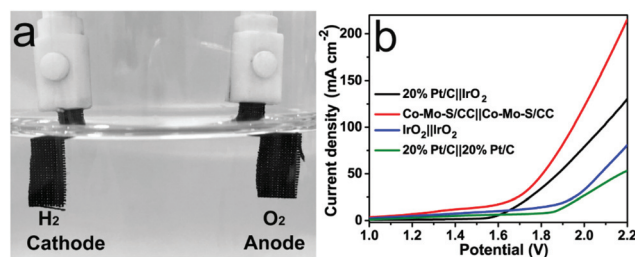


Fig. 5 (a) Photograph of overall water splitting setup in 1 M KOH using Co-Mo-S/CC as both anode and cathode. (b) LSV curves of overall water electrolysis for 20% Pt/C||IrO<sub>2</sub>, Co-Mo-S/CC||Co-Mo-S/CC, IrO<sub>2</sub>||IrO<sub>2</sub> and 20% Pt/C||20% Pt/C.

(4.6 mF cm<sup>-2</sup>). Such low  $R_{ct}$  and high  $C_{dl}$  values of Co-Mo-S/CC should benefit from the active heterostructures with easily accessible active sites.

Motivated by the active HER and OER performances in alkaline electrolyte, Co-Mo-S/CC was evaluated in a two-electrode water splitting electrolyzer as both anode and cathode (Fig. 5a). Co-Mo-S/CC||Co-Mo-S/CC exhibits a small onset potential, and quickly increased current density to simultaneously release bubbles of H<sub>2</sub> and O<sub>2</sub> (Video S1†). In particular, Co-Mo-S/CC||Co-Mo-S/CC requires potential of only 1.80 V to achieve high current density of 50 mA cm<sup>-2</sup>, which is even better than that of commercial 20% Pt/C||IrO<sub>2</sub> (Fig. 5b). The overpotential (570 mV *vs.* RHE) for overall water splitting is also very close to the voltage difference ( $\Delta V$ ) between HER and OER on Co-Mo-S/CC at 50 mA cm<sup>-2</sup> (565 mV). For comparison with the same electrode used as both anode and cathode, IrO<sub>2</sub>||IrO<sub>2</sub> requires the large potential of 2.07 V to afford 50 mA cm<sup>-2</sup> and 20% Pt/C||20% Pt/C gives the potential of 2.16 V at 50 mA cm<sup>-2</sup>. Moreover, Ni-Mo-S/CC as both cathode and anode requires potential of 1.89 V to reach the current density of 50 mA cm<sup>-2</sup>, while the Fe-Mo-S/CC electrode needs 2.09 V to yield 50 mA cm<sup>-2</sup> (Fig. S23, ESI†). The overall water splitting performances of M-Mo-S/CC are in accordance with their relevant HER and OER properties. Therefore, the overall water splitting performance of Co-Mo-S/CC||Co-Mo-S/CC is much better than those of contrast samples and is superior to most of the reported sulfide-based and other non-noble metal-based materials (Table S6†).

## Conclusions

In summary, MoS<sub>2</sub>-based bimetallic sulfides including Co-Mo-S/CC, Ni-Mo-S/CC and Fe-Mo-S/CC were synthesized by a one-pot hydrothermal method using Anderson-type POMs as bimetallic sources. M-Mo-S/CC with its unique morphology and structure was an ideal model for studying the growth mechanism of MoS<sub>2</sub>-based bimetallic sulfides through nucleation-doping competition. Co-Mo-S and Ni-Mo-S nanospheres have heterostructures with CoS<sub>2</sub> or NiS mainly inside and MoS<sub>2</sub> nanosheets outside due to the faster nucleation rate of transition metal sulfides than that of MoS<sub>2</sub>. Identical nuclea-



tion rate of FeS and MoS<sub>2</sub> in Fe–Mo–S is the reason for the formation the uniform structure without stacking into spheres. Moreover, M–Mo–S/CC exhibit excellent electrocatalytic performances for water splitting in alkaline electrolyte. In particular, Co–Mo–S/CC shows low  $\eta_{10}$  of 118 and 300 mV *vs.* RHE and enhanced stability for HER and OER. The two-electrode electrolyzer using Co–Mo–S/CC as both anode and cathode obtains current density of 50 mA cm<sup>−2</sup> at the potential of 1.80 V. The outstanding electrocatalytic performance of Co–Mo–S/CC can be attributed to the following aspects: (1) the homogeneous Co–Mo–S particles grown on CC increase the surface area and expose the active sites to facilitate the electrocatalytic reaction in harsh electrolytes; (2) the hybridization of CoS<sub>2</sub> inside and MoS<sub>2</sub> outside to form stable Co–Mo–S heterostructure ensures improved activity and stability toward both HER and OER; (3) CC substrate possesses woven networks and good electrical conductivity, making it a favorable platform for growing sulfides uniformly and for transferring electrons easily. In brief, together with the facile one-pot hydrothermal method, bimetallic sulfides can be synthesized using POM precursors with fixed metal sources to study the growth mechanism and energy conversion and storage.

## Experimental

### Synthesis of M–Mo–S/CC

Carbon cloth was first treated with water, ethanol and concentrated nitric acid for 30 min sequentially to remove residual organic species. CoMo<sub>6</sub> (0.12 g, 0.1 mmol) and thiourea (0.18 g, 2.4 mmol) were dissolved in 35 mL water by sonication for 30 min to form a homogenous solution. Then, the solution was transferred to a 50 mL Teflon-lined stainless-steel autoclave with two pieces of treated 1 × 2 cm<sup>2</sup> CC added to the solution. The reaction was carried out at 200 °C for 24 h. The resultant Co–Mo–S/CC was washed and sonicated several times using water, followed by drying at 60 °C overnight. The mass loading of Co–Mo–S on CC was ~1 mg cm<sup>−2</sup>. The preparatory processes of Ni–Mo–S/CC, Fe–Mo–S/CC and MoS<sub>2</sub>/CC are similar to that of Co–Mo–S/CC, except that NiMo<sub>6</sub> (0.12 g, 0.1 mmol), FeMo<sub>6</sub> (0.12 g, 0.1 mmol) and Na<sub>2</sub>MoO<sub>4</sub>·2H<sub>2</sub>O (0.145 g, 0.6 mmol) were respectively used as the metal precursor.

### Physicochemical characterization

Powder X-Ray diffraction (PXRD) patterns were recorded on a D/max 2500VL/PC diffractometer (Japan) equipped with graphite monochromatized Cu K<sub>α</sub> radiation ( $\lambda = 1.54060$  Å). The corresponding working voltage and current are 40 kV and 100 mA, respectively. Transmission electron microscopy (TEM) and high-resolution TEM (HRTEM) were carried out on a JEOL-2100F apparatus at an accelerating voltage of 200 kV. Morphology and microstructure analyses were conducted using a scanning electron microscope (SEM, JSM-7600F) at an acceleration voltage of 10 kV. Energy dispersive X-ray spectroscopy (EDS) was performed with a JSM-5160LV-Vantage type

energy spectrometer. The metal molar ratio was determined by inductively coupled plasma atomic emission spectrometry (ICP, Prodigy). HADDF images and element mappings were recorded using an image aberration-corrected TEM (Titan3 G2 60-300) at an acceleration voltage of 300 kV. X-ray photoelectron spectra (XPS) were collected on a scanning X-ray microprobe (PHI 5000 Versa, ULAC-PHI, Inc.) using Al-K<sub>α</sub> radiation with the C 1s peak at 284.8 eV as the internal standard. Raman spectra of powder samples were obtained on a Lab-RAM HR800 with laser excitation wavelength of 532 nm. Fourier transform infrared spectroscopy (FT-IR) was collected on a Nexus 670 spectrometer. Nitrogen adsorption-desorption isotherms were collected at 77 K on a Quantachrome Instruments Autosorb AS-6B.

### Electrochemical measurements

Both HER and OER tests were performed in a three-electrode system on an electrochemical station (Bio-Logic SP-150) using SCE and graphite rod (Sigma-Aldrich, 99.995% trace metals basis) as the reference and counter electrodes, respectively. M–Mo–S/CC and MoS<sub>2</sub>/CC were directly used as the working electrode with geometric surface area of 1 cm<sup>2</sup>. Commercial 20% Pt/C or IrO<sub>2</sub> was first sonicated in ethanol solution mixed with 0.5 wt% Nafion to obtain the concentration of 10 mg mL<sup>−1</sup>. Then 100  $\mu$ L dispersion was drop-casted on CC with mass loading of 1 mg cm<sup>−2</sup> (the coating area is about 1 cm<sup>2</sup>). All LSV curves were measured at the scan rate of 5 mV s<sup>−1</sup> in N<sub>2</sub>-saturated 1 M KOH and corrected for the 85% *i*R-compensation. The Tafel slope was calculated according to the Tafel equation ( $\eta = b \log j + a$ , where  $\eta$  is the overpotential,  $j$  is the current density and  $b$  is the Tafel slope). For LSV stability tests, CV curves were recorded from 0 to −0.2 V *vs.* RHE for HER and from 1.3 to 1.5 V *vs.* RHE for OER at the scan rate of 100 mV s<sup>−1</sup>. EIS measurements were performed at the overpotential of 150 mV *vs.* RHE for HER and 300 mV *vs.* RHE for OER from 10 mHz to 1000 kHz with AC voltage of 10 mV. To estimate ECSA, CV was tested at potential from −0.2 to −0.1 V *vs.* RHE with different scan rates (10, 20, 40, 60, 80 and 100 mV s<sup>−1</sup>). For overall water splitting electrolysis, Co–Mo–S/CC was directly used as both cathode and anode in 1 M KOH. The LSV curves were recorded at the scan rate of 5 mV s<sup>−1</sup>. RHE calibration was performed using the Nernst equation:  $E_{\text{RHE}} = E_{\text{SCE}} + 0.059\text{pH} + E_{\text{SCE}}^{\theta}$ . In 0.5 M H<sub>2</sub>SO<sub>4</sub>,  $E_{\text{RHE}} = E_{\text{SCE}} + 0.245$  V. In 1 M KOH,  $E_{\text{RHE}} = E_{\text{SCE}} + 1.07$  V. In 0.5 M PBS,  $E_{\text{RHE}} = E_{\text{SCE}} + 0.65$  V.

## Conflicts of interest

There are no conflicts to declare.

## Acknowledgements

This study was financially supported by NSFC (No. 21622104, 21471080 and 2170010097), the NSF of Jiangsu Province of China (No. SBK2017040708), the Natural Science Research of



Jiangsu Higher Education Institutions of China (No. 17KJB150025), Priority Academic Program Development of Jiangsu Higher Education Institutions and the Foundation of Jiangsu Collaborative Innovation Center of Biomedical Functional Materials, the Postgraduate Research & Practice Innovation Program of Jiangsu Province (No. KYCX17\_1060).

## Notes and references

- M. S. Dresselhaus and I. L. Thomas, *Nature*, 2001, **414**, 332–337.
- M. G. Walter, E. L. Warren, J. R. McKone, S. W. Boettcher, Q. Mi, E. A. Santori and N. S. Lewis, *Chem. Rev.*, 2010, **110**, 6446–6473.
- L. Han, S. Dong and E. Wang, *Adv. Mater.*, 2016, **28**, 9266–9291.
- C. C. L. McCrory, S. Jung, J. C. Peters and T. F. Jaramillo, *J. Am. Chem. Soc.*, 2013, **135**, 16977–16987.
- Y. Pi, N. Zhang, S. Guo, J. Guo and X. Huang, *Nano Lett.*, 2016, **16**, 4424–4430.
- C. C. L. McCrory, S. Jung, I. M. Ferrer, S. M. Chatman, J. C. Peters and T. F. Jaramillo, *J. Am. Chem. Soc.*, 2015, **137**, 4347–4357.
- J. Liu, Y. Yang, B. Ni, H. Li and X. Wang, *Small*, 2017, **13**, 1602637–1602642.
- Y. Wu, G.-D. Li, Y. Liu, L. Yang, X. Lian, T. Asefa and X. Zou, *Adv. Funct. Mater.*, 2016, **26**, 4839–4847.
- Z.-Y. Yu, Y. Duan, M.-R. Gao, C.-C. Lang, Y.-R. Zheng and S.-H. Yu, *Chem. Sci.*, 2016, **8**, 968–973.
- Z.-H. Xue, H. Su, Q.-Y. Yu, B. Zhang, H.-H. Wang, X.-H. Li and J.-S. Chen, *Adv. Energy Mater.*, 2017, **7**, 1602355–1602361.
- X. Xiao, C.-T. He, S. Zhao, J. Li, W. Lin, Z. Yuan, Q. Zhang, S. Wang, L. Dai and D. Yu, *Energy Environ. Sci.*, 2017, **10**, 893–899.
- Y. P. Zhu, T. Y. Ma, M. Jaroniec and S. Z. Qiao, *Angew. Chem., Int. Ed.*, 2017, **56**, 1324–1328.
- Y. Jin, H. Wang, J. Li, X. Yue, Y. Han, P. K. Shen and Y. Cui, *Adv. Mater.*, 2016, **28**, 3785–3790.
- C. Hu and L. Dai, *Adv. Mater.*, 2017, **29**, 1604942–1604950.
- X. Zhang, Z. Lai, C. Tan and H. Zhang, *Angew. Chem., Int. Ed.*, 2016, **55**, 8816–8838.
- G. Zhang, H. Liu, J. Qu and J. Li, *Energy Environ. Sci.*, 2016, **9**, 1190–1209.
- B. Hinnemann, P. G. Moses, J. Bonde, K. P. Jørgensen, J. H. Nielsen, S. Hørch, I. Chorkendorff and J. K. Nørskov, *J. Am. Chem. Soc.*, 2005, **127**, 5308–5309.
- J. Wang, M. Yan, K. Zhao, X. Liao, P. Wang, X. Pan, W. Yang and L. Mai, *Adv. Mater.*, 2017, **29**, 1604464–1604469.
- Y.-J. Tang, Y. Wang, X.-L. Wang, S.-L. Li, W. Huang, L.-Z. Dong, C.-H. Liu, Y.-F. Li and Y.-Q. Lan, *Adv. Energy Mater.*, 2016, **6**, 1600116–1600122.
- F. K. Perkins, A. L. Friedman, E. Cobas, P. M. Campbell, G. G. Jernigan and B. T. Jonker, *Nano Lett.*, 2013, **13**, 668–673.
- H. Li, Z. Yin, Q. He, H. Li, X. Huang, G. Lu, D. W. H. Fam, A. I. Y. Tok, Q. Zhang and H. Zhang, *Small*, 2012, **8**, 63–67.
- X.-Y. Yu, Y. Feng, Y. Jeon, B. Guan, X. W. Lou and U. Paik, *Adv. Mater.*, 2016, **28**, 9006–9011.
- H. Wang, C. Tsai, D. Kong, K. Chan, F. Abild-Pedersen, J. K. Nørskov and Y. Cui, *Nano Res.*, 2015, **8**, 566–575.
- D. Merki, H. Vrubel, L. Rovelli, S. Fierro and X. Hu, *Chem. Sci.*, 2012, **3**, 2515–2525.
- K. Zhang, S. Feng, J. Wang, A. Azcatl, N. Lu, R. Addou, N. Wang, C. Zhou, J. Lerach and V. Bojan, *Nano Lett.*, 2015, **15**, 6586–6591.
- Y. Guo, L. Gan, C. Shang, E. Wang and J. Wang, *Adv. Funct. Mater.*, 2017, **27**, 1602699–1602705.
- Y. Guo, J. Tang, H. Qian, Z. Wang and Y. Yamauchi, *Chem. Mater.*, 2017, **29**, 5566–5573.
- Y. Yang, K. Zhang, H. Lin, X. Li, H. C. Chan, L. Yang and Q. Gao, *ACS Catal.*, 2017, **7**, 2357–2366.
- J. Zhang, T. Wang, P. Liu, S. Liu, R. Dong, X. Zhuang, M. Chen and X. Feng, *Energy Environ. Sci.*, 2016, **9**, 2789–2793.
- J. Miao, F.-X. Xiao, H. B. Yang, S. Y. Khoo, J. Chen, Z. Fan, Y.-Y. Hsu, H. M. Chen, H. Zhang and B. Liu, *Sci. Adv.*, 2015, **1**, e1500259.
- D.-L. Long, R. Tsunashima and L. Cronin, *Angew. Chem., Int. Ed.*, 2010, **49**, 1736–1758.
- K. Nomiya, T. Takahashi, T. Shirai and M. Miwa, *Polyhedron*, 1987, **6**, 213–218.
- N. Jiang, B. You, M. Sheng and Y. Sun, *Angew. Chem., Int. Ed.*, 2015, **54**, 6251–6254.
- T. Liu, X. Ma, D. Liu, S. Hao, G. Du, Y. Ma, A. M. Asiri, X. Sun and L. Chen, *ACS Catal.*, 2017, **7**, 98–102.
- S. Huang, Y. Meng, S. He, A. Goswami, Q. Wu, J. Li, S. Tong, T. Asefa and M. Wu, *Adv. Funct. Mater.*, 2017, **27**, 1606585–1606594.
- J. Huang, D. Hou, Y. Zhou, W. Zhou, G. Li, Z. Tang, L. Li and S. Chen, *J. Mater. Chem. A*, 2015, **3**, 22886–22891.
- J. G. Speight, *Lange's handbook of chemistry*, McGraw-Hill, New York, 2005.
- L.-L. Long, J.-J. Chen, X. Zhang, A.-Y. Zhang, Y.-X. Huang, Q. Rong and H.-Q. Yu, *NPG Asia Mater.*, 2016, **8**, e263.
- X. Zhang, S. Liu, Y. Zang, R. Liu, G. Liu, G. Wang, Y. Zhang, H. Zhang and H. Zhao, *Nano Energy*, 2016, **30**, 93–102.
- L.-L. Feng, G. Yu, Y. Wu, G.-D. Li, H. Li, Y. Sun, T. Asefa, W. Chen and X. Zou, *J. Am. Chem. Soc.*, 2015, **137**, 14023–14026.
- J. Staszak-Jirkovsky, C. D. Malliakas, P. P. Lopes, N. Danilovic, S. S. Kota, K.-C. Chang, B. Genorio, D. Strmcnik, V. R. Stamenkovic, M. G. Kanatzidis and N. M. Markovic, *Nat. Mater.*, 2016, **15**, 197–203.
- W. Zhao, C. Zhang, F. Geng, S. Zhuo and B. Zhang, *ACS Nano*, 2014, **8**, 10909–10919.
- C. Zhang, Y. Liu, Y. Chang, Y. Lu, S. Zhao, D. Xu, Z. Dai, M. Han and J. Bao, *ACS Appl. Mater. Interfaces*, 2017, **9**, 17326–17336.
- Y.-J. Tang, M.-R. Gao, C.-H. Liu, S.-L. Li, H.-L. Jiang, Y.-Q. Lan, M. Han and S.-H. Yu, *Angew. Chem., Int. Ed.*, 2015, **54**, 12928–12932.